# *In Situ* Phase Transformation on Nickel-Based Selenides for Enhanced Hydrogen Evolution Reaction in Alkaline Medium

Lingling Zhai[1], Tsz Woon Benedict Lo[2], Zheng-Long Xu[1, 5], Jonathan Potter[3], Jiaying Mo[4], Xuyun Guo[1], Chiu Chung Tang[3], Shik Chi Edman Tsang[4], Shu Ping Lau[1*]

1 Department of Applied Physics, The Hong Kong Polytechnic University, Hung Hom, Hong Kong, China

2 State Key Laboratory of Chemical Biology and Drug Discovery, Department of Applied Biology and Chemical Technology, The Hong Kong Polytechnic University, Hung Hom, Hong Kong, China

3 Diamond Light Source Ltd, Harwell Science and Innovation Campus, Didcot, Oxford OX11 0DE, U.K

4 The Wolfson Catalysis Centre, Department of Chemistry, University of Oxford, Oxford OX1 3QR, U.K

5 Department of Industrial and Systems Engineering, The Hong Kong Polytechnic University, Hung Hom, Hong Kong, China

* Corresponding author.

Email address: apsplau@polyu.edu.hk (S.P. Lau).

**Abstract**

Identification of the active species in electrocatalysts toward hydrogen evolution reaction (HER) is of great significance for the development of catalytic industry, while it still endures considerable controversy. Herein, we applied *operando* synchrotron X-ray powder diffraction (SXRD) in the $NiSe_2$ electrocatalyst system, an *in situ* phase transformation from cubic $NiSe_2$ to hexagonal NiSe was revealed. The NiSe phase showed an enhanced catalytic activity. *Operando* Raman spectroscopy verified the decomposition of $NiSe_2$ during HER. Theoretical calculations suggested that the charge transfers from Se site to Ni site during this evolution process, leading to an increased conductivity and a shifting up of *d*-band center, which attributed to the enhanced activity. The generated NiSe phase is acted as the "real" active species. Our work unravels the underlying phase transition of electrocatalyst on reductive conditions in alkaline medium and highlights the significance of identifying the intrinsic active sites under realistic reaction conditions.

Due to the limited source of fossil fuels and the increasing environmental contaminations, large-scale production of hydrogen fuel from water splitting is considered as a promising alternative strategy for green energy generation.[1-3] Although platinum is recognized as the most efficient catalyst for HER, the high cost and scarcity severely impede its extensive application.[4, 5] In the last several decades, significant efforts have been made to develop non-precious metal electrocatalysts, among which includes a large family of transition-metal chalcogenides[6, 7] and phosphides.[8-10] Due to the metalloid property of sulfur, selenium and phosphorus, these compounds show narrow band gaps or metallic conductivities which facilitate the electron transportation. Accordingly, some of them have shown superior electrocatalytic performance in alkaline water splitting and possess huge potential in commercial utilization. Nevertheless, the underlying mechanism for HER are still under considerable debate, the understanding of the electrocatalytic process and the identification of the real active sites are still lacking, especially when compared with the rather well explored oxygen evolution reaction (OER) process.[11-13]

The transition-metal based catalysts have been regarded stable for HER when compared with the harsh OER conditions. Until very recently, it was noticed that some catalysts may experience a structural reorganization or phase evolution during the reduction process. For instance, $NiS_2$-based electrocatalysts were considered durable for alkaline HER.[14, 15] However, it was reported that $NiS_2$ could be reduced into metallic Ni, which acted as the real active site for hydrogen generation.[16, 17] Similarly, by applying comprehensive post-catalytic measurements, $Co_2P$ was observed to degrade into hydroxide after a prolonged HER.[18] Nevertheless, it should be cautious that sample oxidation due to the ambient exposure could not be excluded. From this perspective, the conventional *ex-situ* techniques are not capable of qualitatively identify the active catalysts, let alone dynamically

capture the structural or compositional transformation under working conditions. In contrast, *operando* or *in-situ* methods are emerging as indispensable tools to track the self-reorganization process and to reveal the active sites. Recently, a P-substituted $CoSe_2$ was found to reduce into metallic cobalt which acted as the active site for HER.[19] Our previous research also confirmed the morphological and compositional changes of $NiSe_2$ after both HER and OER.[20] Due to the limitation of *ex-situ* characterization tools, it is urgently needed to employ *operando* instruments to track the phase evolution and identify the active sites of these electrocatalysts.

In this work, we developed an electrochemical cell which can measure the evolution of the SXRD pattern of the $NiSe_2$ electrocatalyst toward HER under *operando* conditions. The dynamic structural and compositional transformation from cubic $NiSe_2$ (JCPDS no. 65-1843) to hexagonal NiSe (JCPDS no. 65-3425) under a series of reductive conditions were revealed. Through this self-reorganized phase transformation process, the current density of the electrocatalyst could be increased by 27.3%. Then, *Operando* Raman spectroscopy further confirmed the decomposition of $NiSe_2$. Moreover, a phase evolution mechanism was proposed with the combination of *ex-situ* measurements such as high-resolution transmission electron microscopy (HRTEM) and X-ray photoelectron spectroscopy (XPS). Additionally, the density functional theory (DFT) studies further revealed the increase in conductivity and the raising up of *d*-band center, which leads to the enhancement of catalytic activity. Our work provides new insights into the chemical and physical transformation of the electrocatalyst during the electrochemical process. It may enable the development of the high-efficient and stable electrocatalysts for hydrogen production.

The $NiSe_2$ nanoparticles were synthesized through a thermal selenization method with carbon paper (CP) as substrates (see details in Supporting Information). As shown in **Figure S1a**, the NiO

nanoparticles were anchored onto the carbon fiber and the pristine carbon fiber shows a smooth cylindric surface with a diameter of ~10 μm (**Figure S1b**). After selenization, the morphology is well conserved as shown in **Figure 1a**. Powder X-ray diffraction (XRD, **Figure S2**) patterns reveal the compositional change from NiO (JCPDS no. 65-2901) to $NiSe_2$. The narrow and sharp peaks reflect the highly crystalline nature of the $NiSe_2$, which is further confirmed by the HRTEM results. As shown in **Figure 1b**, the large domain presents a typical surface of (210) phase. The lattice *d*-spacings of 2.7 Å, 3.0 Å and 6.0 Å are also consistent with the values of (210), (200) and (010) planes, respectively. Moreover, the energy-dispersive X-ray (EDX) elemental mapping (**Figure 1c**) reveals the homogeneous distribution of Ni and Se throughout the particle with a Se/Ni atomic ratio of 2.17. The slight excess Se derives from the absorbed species on its surface.[19, 21] For better comparison, $Ni(OH)_2$ was also prepared by an electrodeposition method (see details in Supporting Information). As shown in **Figure S3**, the carbon fiber is uniformly covered by the as-prepared $Ni(OH)_2$, the XRD pattern is also consistent with α-$Ni(OH)_2$ (JCPDS no. 38-0715).

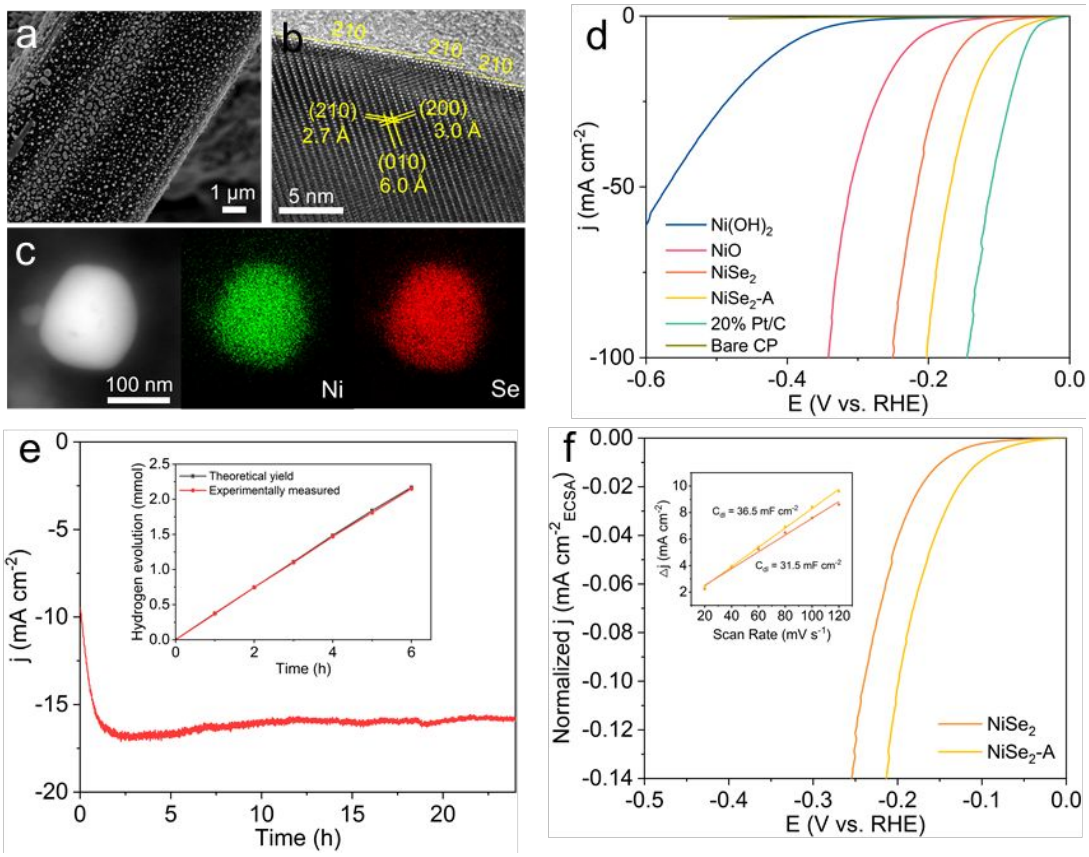


**Figure 1.** (a) SEM image of the $NiSe_2$ nanoparticles. (b) HRTEM image of the $NiSe_2$ nanoparticle. (c) HAADF-STEM image and the corresponding EDX mapping images of the $NiSe_2$. (d) LSV polarization curves of the $Ni(OH)_2$, NiO, $NiSe_2$, $NiSe_2$-A, 20% Pt/C and bare CP in 1 M KOH. (e) Chronoamperometric curve of the $NiSe_2$ at -0.16 V for 24 h. Inset: theoretical and experimentally measured volumes of $H_2$ as a function of time for $NiSe_2$-A. (f) ESCA-normalized LSV polarization curves of the $NiSe_2$ and $NiSe_2$-A. Inset: $C_{dl}$ values of $NiSe_2$ and $NiSe_2$-A.

The electrochemical behavior of the as-prepared $NiSe_2$ toward HER was first examined in 1M KOH by linear sweep voltammetry (LSV). $Ni(OH)_2$, NiO, commercial 20% Pt/C and bare CP were also tested as reference catalysts. Before test, the fresh $NiSe_2$ was immersed in the electrolyte without any potential for 12 h and examined by XRD. As shown in **Figure S4**, the patterns show no obvious difference, confirming the stability of $NiSe_2$ in KOH without potential. The LSV curves were obtained at a scan rate of 5 mV $s^{-1}$ after the initial cyclic voltammetry (CV) for 20 cycles at a scan rate of 50 mV $s^{-1}$. As shown in **Figure 1d**, the bare CP shows negligible activity while the 20 % Pt/C demonstrates a lowest overpotential of 65 mV to reach a current density (j) of -10 mA $cm^{-2}$ ($\eta_{10}$ = 65 mV). As compared to the $Ni(OH)_2$ and NiO with poor catalytic activities ($\eta_{10}^{Ni(OH)_2}$=

411 mV, $\eta_{10}^{NiO}$ = 232 mV), the $NiSe_2$ exhibits much superior performance, as indicated by the largely decreased overpotential ($\eta_{10}$ = 157 mV). To further evaluate the stability of the $NiSe_2$ catalyst, chronoamperometry measurement was conducted at a constant potential of -0.16 V (initial current density ~ -10 mA $cm^{-2}$) for 24 h. As shown in **Figure 1e**, the current density shows negligible degradation, indicating excellent stability of the sample. Interestingly, the current density was found to gradually increase from -9.5 mA $cm^{-2}$ to -16.7 mA $cm^{-2}$ in the first two hours. This phenomenon is also verified by the increased activity with increasing cycling number as shown in **Figure S5**. These facts indicate a probable electrochemical activation process of the $NiSe_2$ nanoparticles during alkaline HER.[22, 23]

To further investigate the performance of the catalyst after deep activation, the sample after two hours' chronoamperometry is denoted as $NiSe_2$-A. As revealed in the polarization curves (**Figure 1d**), the $NiSe_2$-A achieves a current density of -93 mA $cm^{-2}$ at an overpotential of 0.2 V, which is three times higher than that of $NiSe_2$ at the same overpotential, indicating a much enhanced catalytic activity after fully activation. Additionally, the corresponding Tafel plots were also investigated to gain kinetic insights into the HER process (**Figure S6**). The $NiSe_2$-A catalyst achieves the lowest value of Tafel slope (76 mV $dec^{-1}$) as compared with that of $Ni(OH)_2$ (134 mV $dec^{-1}$), NiO (94 mV $dec^{-1}$) and $NiSe_2$ (79 mV $dec^{-1}$), demonstrating the rapid HER rate after activation. The Faradaic efficiency (FE) of the $NiSe_2$-A during alkaline HER was also calculated to be 99% (**Figure 1e** inset). Furthermore, the turnover frequencies (TOFs) of the above-mentioned nickel-based electrocatalysts were evaluated by assuming that all nickel atoms in the materials were catalytically active (**Figure S7**). The TOF of $NiSe_2$-A is $8.6 \times 10^{-2}$ $s^{-1}$ at $\eta$ = 210 mV, which is much larger than that of $Ni(OH)_2$ ($1.2 \times 10^{-4}$ $s^{-1}$), NiO ($1.5 \times 10^{-3}$ $s^{-1}$) and $NiSe_2$ ($3.3 \times 10^{-2}$ $s^{-1}$). The higher TOF value of $NiSe_2$-A suggests enhanced intrinsic catalytic activity. To gain further

insight into the charge transfer behavior at the interface of the catalyst and the electrolyte, the electrochemical impedance spectroscopy (EIS) was performed (all parameters were listed in **Table S1**). As shown in **Figure S8**, the Nyquist plot of $NiSe_2$-A reveals a lowest charge transfer resistance ($R_{ct}$) value of 1.97 Ω, suggesting the superior charge transfer property after activation.

The electrocatalytic performance of the electrode is largely affected by the electrochemical surface area (ECSA). To eliminate the effect of surface coarseness, ECSA values were calculated from the corresponding double-layer capacitance ($C_{dl}$) (see details in Supporting Information). The $C_{dl}$ values were obtained from CV at different scan rates in the non-faradaic region as shown in **Figure S9**. The ECSA-normalized polarization curves are shown in **Figure 1f** to reveal the intrinsic activity after activation. Clearly, the $C_{dl}$ value is slightly increased after activation, the enhanced activity of the $NiSe_2$-A indicates that, in addition to the higher active surface area, the intrinsic catalytic activity of the catalyst is also improved by the activation process.

In order to explore the underlying activation process of the $NiSe_2$ during HER in alkaline medium, an *operando* high-resolution SXRD characterization was conducted. **Figure S10** shows the experimental set up. The synchrotron data was collected using a pixel area detector in transmission geometry. The $NiSe_2$ catalyst was applied at a constant potential of -0.18 V for 6 h, i-t curve and time-resolved diffraction patterns were collected *in operando* as shown in **Figure 2a**. The current density of the $NiSe_2$ is -16.2 mA $cm^{-2}$ at the beginning and gradually increased by 27.3% in the first 2 h. Meanwhile, the characteristic peaks of the cubic $NiSe_2$ at 10.7° (210), 13.6° (220) and 15.9° (311) are shown but gradually decrease in intensity as the reaction progresses. Then after 2 h, the current density reaches 20.5 mA $cm^{-2}$ and remains unchanged. At the same time, three new diffraction peaks at 10.4°, 14.0° and 15.6° become prominent in the SXRD patterns as shown in **Figure 2b-g**, which are the characteristic peaks for the hexagonal NiSe phase. These can be readily

identified as (011), (012) and (110) reflection, respectively. Interestingly, the increasing of the NiSe peaks is at the expense of the $NiSe_2$ peaks, signifying a phase transformation from cubic $NiSe_2$ to hexagonal NiSe. The background-subtracted diffraction patterns as a function of reaction time are shown in **Figure S11a**. By refining the synchrotron data using *TOPAS* analytical software, we obtained the lattice parameters of the NiSe phase (**Table S2**). As the electrochemical reaction progress, the NiSe unit cell contracts along the *a*-axis but expands along *c*-axis. It suggests compressing forces on the *b*-*c* surface and drawing forces on the a-*b* surface, which can be ascribed to the electric stress and the interaction with the neighbor $NiSe_2$ nanocrystallites or domains. The chronoamperometry measurement was prolonged for 24 h, the corresponding SXRD pattern is shown in **Figure S11b**. Clearly, the characteristic peaks of the NiSe show no obvious change after 2 h while the characteristic peaks of the $NiSe_2$ keep declining until almost undetectable. This result confirms the completely decomposition of the $NiSe_2$. It should be noted that the phase evolution after 2 h did not reveal obvious influence on the HER performance, thus we suppose the major evolution occurred in the first 2 h. We also noticed that the transparent electrolyte changed into red after the reaction (**Figure S12a**). Then, the electrolyte was filtrated and a thin layer of red precipitate was collected as shown in **Figure S12b-c**. Raman spectra of the precipitate shows peaks at 146.8 $cm^{-1}$ and 242.5 $cm^{-1}$, which matches well with the elemental Se (**Figure S12d**). EDX spectra also confirms the existence of Se (**Figure S13**). Combining with the SXRD results, it can be concluded that the $NiSe_2$ nanoparticles are unstable during alkaline HER and readily disproportionate into NiSe and Se during the reaction ($NiSe_2 \rightarrow NiSe + Se$). For comparison, the *operando* measurement of the NiO during HER was conducted under -0.23 V (current density ~ -10 mA $cm^{-2}$). As shown in **Figure S14**, the current density is decreased due to the degradation of activity, and the characteristic peaks of NiO does not show any change over time, indicating the

unique phase evolution property of the $NiSe_2$ reaction system.

With the aim to further study the phase evolution in higher biased potentials, *operando* SXRD at -0.38 V and – 0.58 V were also conducted. As shown in **Figure S15**, the evolution of the SXRD patterns is similar with previous result (-0.18 V) but with a faster rate. It should be noted that the characteristic peaks of the NiSe at -0.58 V are broader, indicating smaller domains. This change may be due to the drastic electron transportation and environmental stress.

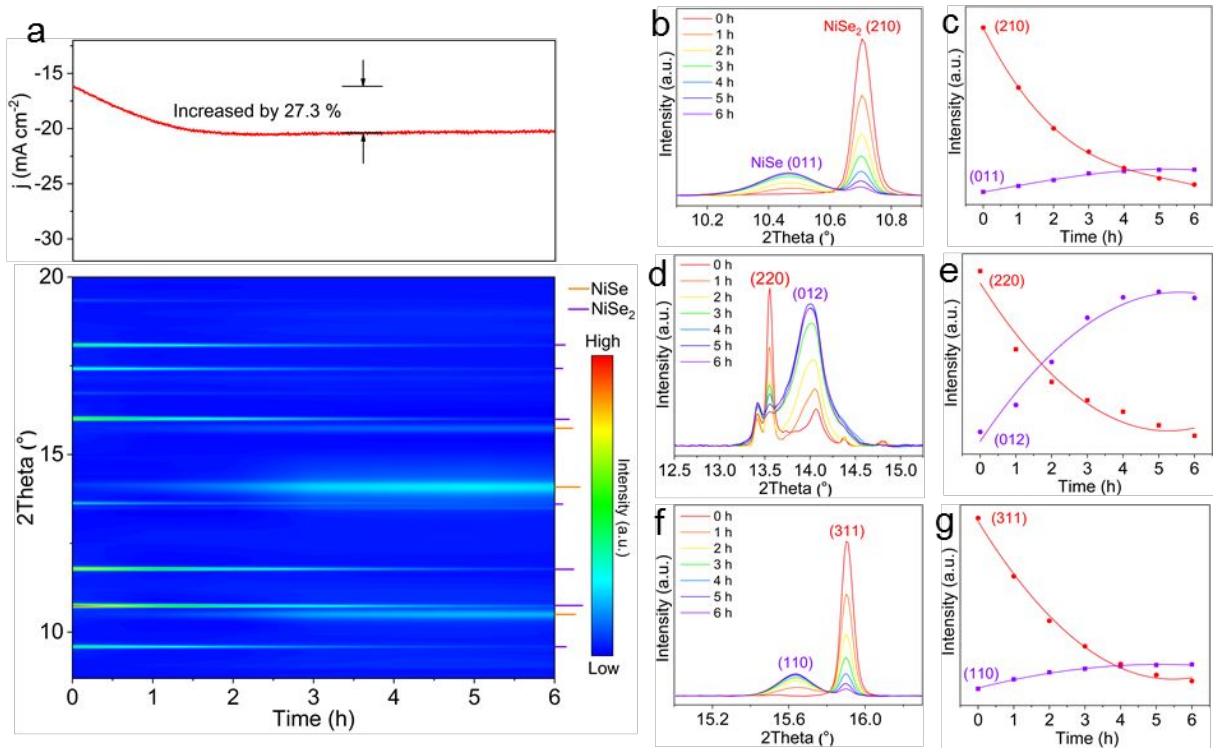


**Figure 2.** (a) Chronoamperometric curve of the $NiSe_2$ at -0.18 V for 6 h and the corresponding operando SXRD patterns ($\lambda$ = 0.49547(1) Å). (b-g) Enlarged characteristic peaks of $NiSe_2$ and NiSe phases and the corresponding intensity variations.

With the aim of revealing the surface states of the $NiSe_2$ electrocatalyst during reaction, *operando* Raman spectroscopy was employed to monitor the real-time evolution using the specially designed setup as shown in **Figure S16**. The bare CP shows no obvious peaks in the range of 100 to 800 $cm^{-1}$ (**Figure S17**), while the as-prepared $NiSe_2$ shows characteristic peaks at 155, 169, 216 and

243 $cm^{-1}$ for $T_g$ (libration), $E_g$ (libration), $A_g$ (stretching) and $T_g$ (stretching) modes, respectively (**Figure 3a**).[24] As the pristine $NiSe_2$ was immersed into deionized (DI) water and KOH, the peak intensity was decreased due to the scattering. Additionally, the relative peak intensity of $T_{g(l)}$ and $A_g$ ($I_T/I_A$) increases from 0.4 to 1.0, indicating a prominent $T_{g(l)}$ mode in liquid. Since this change has already appeared in pure DI water, we suppose it is due to the constrains by the neighboring water molecules. The sample was then characterized under different potentials. The peak intensities are further declined which is due to the structural decomposition of $NiSe_2$, the $I_T/I_A$ value increases to 1.9 when the potential is -0.8 V, confirming the preference of $T_{g(l)}$ mode in liquid. Notably, the $T_{g(l)}$ peak is red shifted to 147 $cm^{-1}$ and the $A_g$ peak is blue shifted to 228 $cm^{-1}$. This result can be attributed to two reasons: i) the charge accumulation on the cathode leads to lattice distortion; ii) the phase evolution from $NiSe_2$ to NiSe leads to an unsymmetrical structural. To further evaluate the time-resolved phase transformation, a constant potential of -0.2 V was applied for 5 h. As shown in **Figure 3b**, the declined intensity of the characteristic peaks confirms the decreasing of $NiSe_2$ quantity, the peak shifting is maintained during the whole process. These findings confirm the decomposition of $NiSe_2$ which is in accordance with the SXRD results.

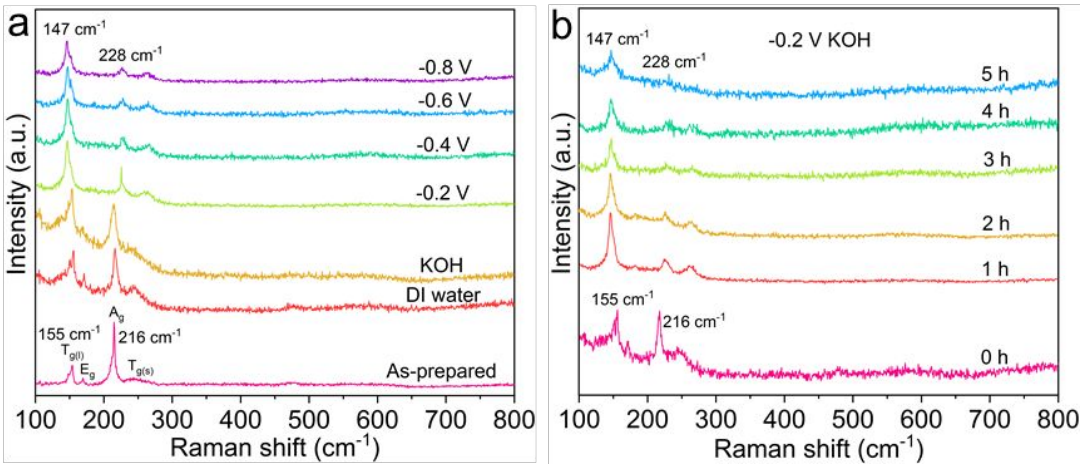


**Figure 3.** (a) *Operando* Raman spectra of the $NiSe_2$ catalyst at various potentials. (b) Time-resolved *operando* Raman spectra of the $NiSe_2$ catalyst at -0.2 V.

To further verify the structural and compositional changes of the $NiSe_2$, *ex-situ* TEM was employed to clarify the time-dependent phase evolution. The reaction time were chosen as 0, 1, 2 and 6 h as compared to the SXRD results. As shown in **Figures 4a** and **b**, the pristine $NiSe_2$ nanoparticle shows smooth surface with a regular round shape. The HRTEM image reveals a (210) reflection, the corresponding selected area electron diffraction (SAED) pattern also shows the highly crystalline nature of the $NiSe_2$. After 1 h of reaction, the edge of the particle becomes coarse and thinner (**Figure 4c**), indicating the structural changes start from the surface. The SAED pattern demonstrates that the $NiSe_2$ is the majority phase. The HRTEM image still shows a (210) reflection of $NiSe_2$, while a (102) reflection of NiSe is captured as shown in **Figure 4d**. This new phase is generated along with the distortion of the lattice in the $NiSe_2$. This heterostructure confirms the early stage of the phase transformation which is consistent with the SXRD results. After 2 h of reaction, the particle structure continues to evolve and becomes irregular (**Figure 4e**). The HRTEM shows multiple orientations containing both $NiSe_2$ and NiSe phases (**Figure 4f**), while the SAED indicates the NiSe phase is increased further (**Figure 4e inset**). Additionally, the SAED pattern exhibits blurry rings rather than the scatted dots, which is due to the multiple small domains. Finally, after 6 h of reaction, the particle is further decomposed with thinner edges (**Figure 4g**), the structure is dominated by the NiSe phase as shown in **Figure 4h**. Meanwhile, the SAED pattern only displays the NiSe phase. Combining the SXRD and TEM results, it can be concluded that during the reaction in alkaline, each crystalline $NiSe_2$ particle (~hundreds of nm) in the bulk gradually transforms into multiple small domains (size ~ tens of nm) with a dominating NiSe phase and a diminishing $NiSe_2$ phase. The phase transformation can be named as "catalytic domaining process" as shown in **Figure 4i**. We speculate that, under cathodic potentials, the charge aggregation on the $Se_2^{2-}$ dimers breaks the Se-Se bonds in $NiSe_2$. Then one of $Se^-$ ions lost an

electron and re-arranged, the other $Se^-$ ion gains an electron and bond with the Ni atom with lattice distortion (cell contraction). This phase evolution is randomly occurred on the particle and is generated multiple phase boundaries (domain structure). While the insight of the precipitation of Se needs more study in the future which is beyond the scope of our work. The changes of atomic ratios of Se/Ni were also examined by EDX as listed in **Table S3**. The value is 2.17 for the pristine $NiSe_2$, while after 6 h of reaction, it reduces to 0.92, which is even lower than that in pure NiSe. This result confirms the large-scale detachment of Se, also suggests the probable Se vacancies. Electron paramagnetic resonance (EPR) was conducted to verify the existence of Se vacancies. As shown in **Figure 4j**, the EPR signals can be found at the *g* value of 2.001, a stronger signal indicates a higher level of Se vacancies.[25, 26] As for pristine $NiSe_2$, the weak signal suggests negligible Se vacancy. After HER, the peak signal is increased as a function of reaction time. This trend is maintained as the reaction time prolonged, indicating the $NiSe_2$/NiSe hybrid is Se vacancy rich. It is well accepted that vacancies and defects are beneficial for the improvement of catalytic activity.[27, 28]

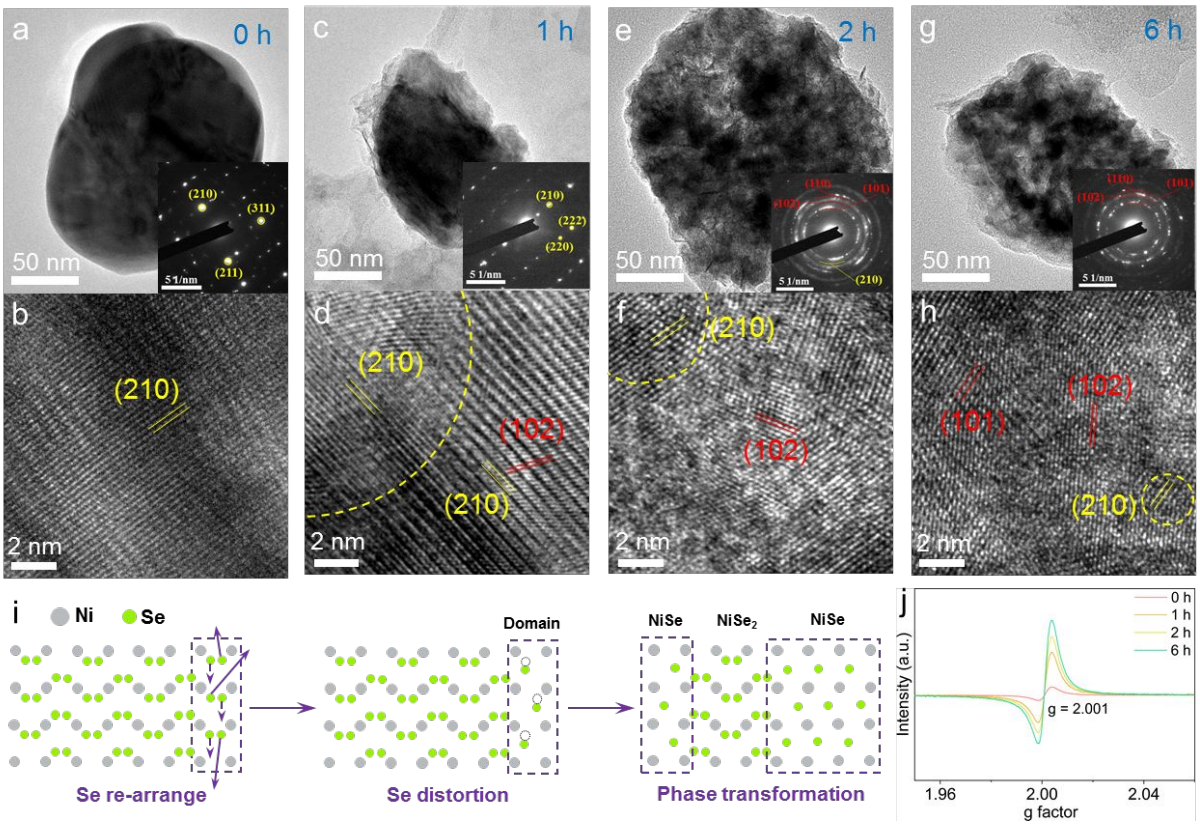


**Figure 4.** TEM images, HRTEM images and the corresponding SAED patterns of (a-b) pristine $NiSe_2$, (c-d) after 1 h, (e-f) 2 h, and (g-h) 6 h of reaction. Yellow and red reflection represents $NiSe_2$ and NiSe phases, respectively. (i) Schematic illustration of the domaining process. (j) EPR spectra of the pristine $NiSe_2$ and after various HER reaction times.

To further investigate the oxidation state of the $NiSe_2$ prior to and post HER, XPS characterization was employed. All the samples were etched by Ar-ion for 60 s to clean the surface. As shown in **Figure 5a**, the pristine $NiSe_2$ shows Ni 2p spectrum at 853.3 eV and 870.5 eV, representing the $Ni^{2+}$ oxidation state.[29] The deconvoluted Ni $2p_{3/2}$ peaks reveal the Ni-Se bond at 853.3 eV and Ni-O bond (due to surface oxidation) at 854.5 eV. These results are consistent with previous studies.[30, 31] After reaction, the bonding energy of Ni-Se is red shifted by 0.5 eV. Based on previous result, the pure $NiSe_2$ has transformed into NiSe (remains a small ratio of $NiSe_2$) with Se vacancies. In viewing that the binding energy of Ni-Se in NiSe is lower than that in $NiSe_2$,[32] it is naturally to consider the peak at 852.7 eV as a mixed state of Ni-Se in the $NiSe_2$/NiSe hybrid. Additionally, the binding energy of Ni-O reveals continuous blue shift, representing the Ni-OH bond[33, 34] which

is caused by the strong KOH electrolyte and Se vacancies. For the pristine Se 3d spectrum (**Figure 5b**), two peaks located at 54.5 eV and 55.5 eV are indexed to Se $3d_{5/2}$ and Se $3d_{3/2}$, matching well with previous report.[29, 34] After reaction, the peaks are red shifted by 0.6 eV, confirming a lower oxidation state. These results are consistent with the TEM results, confirming the phase transformation process.

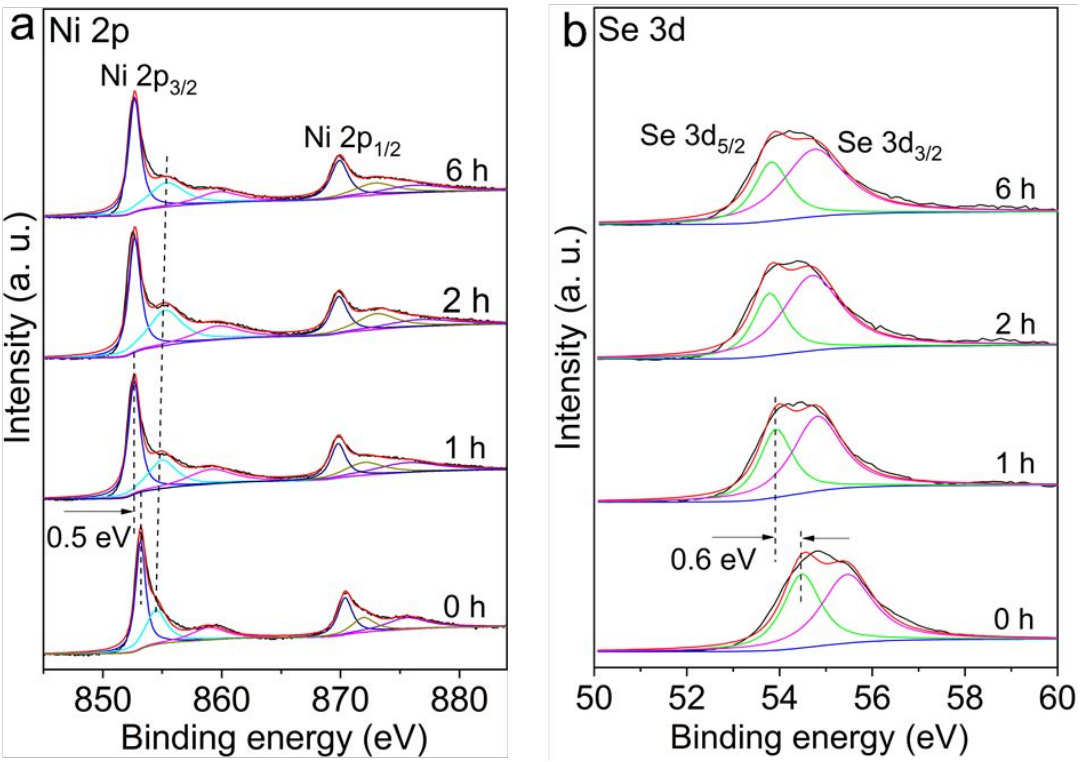


**Figure 5.** XPS spectra of (a) Ni 2p region and (b) Se 3d region as a function of reaction time.

To decipher the modulation essence of the phase transformation in $NiSe_2$ for alkaline HER under atomic level, DFT calculations were further applied. A cell model of $NiSe_{1.5}$ is also constructed as a transition phase, where two Se atoms are taken out from the $NiSe_2$ unit cell. The structures and lattice parameters of $NiSe_2$, $NiSe_{1.5}$ and NiSe are given in **Figure S18** and **Table S4**. The total density of states (DOS) were first calculated as shown in **Figure 6a**, the polyhedral cell structures are given in **Figure 6b**. Partial density of states (PDOS) of Ni *d*-band and Se-*p* band are also given, as they are the main factors that determine the electronic properties.[35, 36] Clearly, the $NiSe_2$ shows

a semiconductor property with a narrow band gap of 0.24 eV, which is consistent with previous reports.[37, 38] Compared with the Ni *d*-band, the Se *p*-band is much more delocalized with a broad width, confirming the strong interaction with the neighbors. In the $NiSe_2$ structure, the Ni 3d orbital owns a fully occupied $t_{2g}$ band and a half-filled $e_g$ band, the Se-Se bond is covalent with pairs of pσ and pπ bondings[36]. Thus we expect, the covalent bonding in the $Se_2^{2-}$ dimer is interrupted due to the negative potential on the cathode. Then partial charge transfers from the Se *p* orbital to the Ni $e_g$ orbital, leading to the rise of the Se *p*-band and crossover the Fermi level. When the crystal further transforms into hexagonal NiSe, the Ni *d*-band also pass through the Fermi level with increased energy in states, which is in accordance with previous literatures.[39, 40] The *d*-band center and occupied electron numbers in Ni *d*-band and Se *p*-band are also calculated as shown in **Table S5**. The *d*-band center[41] is a reasonable descriptor to predict the catalytic activity of transition metals, which is a measure of the strength between metal and absorbate (i.e. hydrogen adsorption energy). Since the *d*-band is much more localized than *sp*-bands in transition metal, the hydrogen adsorption energy depends, to a large extent, on the electronic interaction between the hydrogen *s* states and the metal *d* states, forming bonding and antibonding states. Then a higher *d*-band center of the catalyst leads to a less filled antibonding states, raising up the bonding energy with the hydrogen. An optimized bonding energy should be neither too strong nor too weak. Since Pt is widely accepted as a benchmark among HER catalysts, its *d*-band center position (-1.93 eV vs. Fermi level)[42] is usually regarded as an ideal value. Based on the calculation result, the *d*-band center of Ni is shifted up during the phase transition, which is closer to the position of Pt. This trend matches well with the increased activity in the experiments. Besides, the trends of electron occupancy per atom also show charge accumulations on Ni site and charge depletions on Se site. This result is further confirmed by the charge density difference maps as shown in **Figure 6c**. It is

obvious that the charge accumulates on the Se site in $NiSe_2$ while on the Ni site in NiSe. Based on these results, it can be concluded that the $NiSe_2$ to NiSe phase transformation is accompanied with the charge transfer from Se sites to Ni sites, leading to an improved conductivity and shift up of *d*-band center. This phase evolution results in an enhanced catalytic activity, and the newly generated NiSe species act as the real active site.

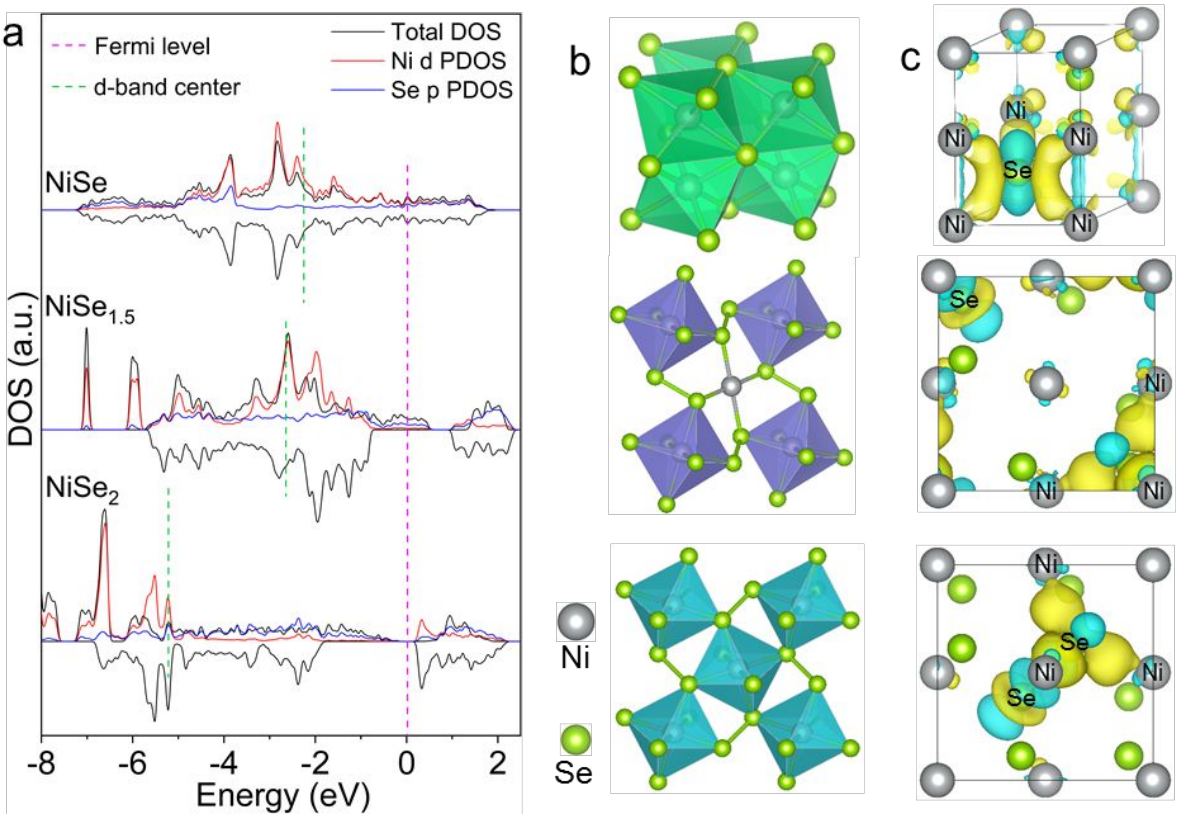


**Figure 6.** (a) The DOS plots of $NiSe_2$, $NiSe_{1.5}$ and NiSe. The Fermi level and the *d*-band center are also highlighted. (b) Polyhedral cell structures of $NiSe_2$, $NiSe_{1.5}$ and NiSe. (c) Isosurfaces of the charge density difference at one Se atom in a unit cell. Yellow and cyan clouds indicate charge gain and loss, respectively. The isosurface is 0.005 e $Bohr^{-3}$.

In summary, the $NiSe_2$ electrocatalyst during alkaline HER was investigated through *operando* SXRD and Raman spectroscopy and other *ex-situ* approaches (SEM, HRTEM, XPS, and DFT calculations). From the synchrotron work, an *in-situ* phase transformation from cubic $NiSe_2$ to hexagonal NiSe was observed during the reaction process. The transformation is supported by the findings in the detailed study of HRTEM imaging and diffraction. From the complementary X-ray

spectroscopic and calculation results, the charge transfer from Se site to Ni site leads to an enhanced conductivity and shifting up of *d*-band center, which contributes to improving the HER performance. Our work provides evidence and information for understanding the fundamental of electrocatalysis and offers insights into the nature of catalytic active sites. We expect this work could inspire more investigations of self-assembled reconstructions beyond $NiSe_2$ system such as other transition metal chalcogenides as these catalytic materials are promising to produce hydrogen energy efficiently in industrial application.

## ASSOCIATED CONTENT

**Supporting Information**. The Supporting Information is available free of charge via the Internet at http://pubs.acs.org. Experimental details, SEM images, XRD patterns, LSV curves, SXRD set-up images, SXRD patterns, Raman spectra, DFT calculations, etc.

## AUTHOR INFORMATION

### Corresponding Author

*apsplau@polyu.edu.hk (S.P. Lau).

### Notes

The authors declare no competing financial interest.

## ACKNOWLEDGMENT

This work was financially supported by the Research Grants Council of Hong Kong (PolyU 253009/18P) and the Hong Kong Polytechnic University (1-ZVGH). The authors acknowledge the facility support from Beamline I11 at Diamond Light Source, UK (proposal no. NT23230).

## REFERENCES

(1) Zhang, Y.; Xia, X.; Cao, X.; Zhang, B.; Tiep, N. H.; He, H.; Chen, S.; Huang, Y.; Fan, H. J., Ultrafine Metal Nanoparticles/N-Doped Porous Carbon Hybrids Coated on Carbon Fibers as Flexible and Binder-Free Water Splitting Catalysts. *Adv. Energy Mater.* **2017,** *7*, 1700220.

(2) Yu, B.; Qi, F.; Zheng, B.; Hou, W.; Zhang, W.; Li, Y.; Chen, Y., Self-Assembled Pearl-Bracelet-Like $CoSe_2$–$SnSe_2$/CNT Hollow Architecture as Highly Efficient Electrocatalysts for Hydrogen Evolution Reaction. *J. Mater. Chem. A* **2018,** *6*, 1655-1662.

(3) Wang, X.; He, J.; Yu, B.; Sun, B.; Yang, D.; Zhang, X.; Zhang, Q.; Zhang, W.; Gu, L.; Chen, Y., $CoSe_2$ Nanoparticles Embedded MOF-Derived Co-N-C Nanoflake Arrays as Efficient and Stable Electrocatalyst for Hydrogen Evolution Reaction. *Appl. Catal. B: Environ.* **2019,** *258*, 117996.

(4) Xu, K.; Ding, H.; Zhang, M.; Chen, M.; Hao, Z.; Zhang, L.; Wu, C.; Xie, Y., Regulating Water-Reduction Kinetics in Cobalt Phosphide for Enhancing HER Catalytic Activity in Alkaline Solution. *Adv. Mater.* **2017,** *29*, 1606980.

(5) Wang, X.; Zheng, B.; Yu, B.; Wang, B.; Hou, W.; Zhang, W.; Chen, Y., In Situ Synthesis of Hierarchical $MoSe_2$–$CoSe_2$ Nanotubes as an Efficient Electrocatalyst for the Hydrogen Evolution Reaction in Both Acidic and Alkaline Media. *J. Mater. Chem. A* **2018,** *6*, 7842-7850.

(6) Fang, Z.; Peng, L.; Qian, Y.; Zhang, X.; Xie, Y.; Cha, J. J.; Yu, G., Dual Tuning of Ni–Co–A (A= P, Se, O) Nanosheets by Anion Substitution and Holey Engineering for Efficient Hydrogen Evolution. *J. Am. Chem. Soc.* **2018,** *140*, 5241-5247.

(7) Li, W.; Yu, B.; Hu, Y.; Wang, X.; Yang, D.; Chen, Y., Core–Shell Structure of $NiSe_2$ Nanoparticles@ Nitrogen-Doped Graphene for Hydrogen Evolution Reaction in Both Acidic and Alkaline Media. *ACS Sustain. Chem. Eng.* **2019,** *7*, 4351-4359.

(8) Xu, K.; Sun, Y. Q.; Sun, Y. M.; Zhang, Y. Q.; Jia, G. C.; Zhang, Q. H.; Gu, L.; Li, S. Z.; Li, Y.; Fan, H. J., Yin-Yang Harmony: Metal and Nonmetal Dual-Doping Boosts Electrocatalytic Activity for Alkaline Hydrogen Evolution. *ACS Energy Lett.* **2018,** *3* (11), 2750-2756.

(9) Parra-Puerto, A.; Ng, K. L.; Fahy, K.; Goode, A. E.; Ryan, M. P.; Kucernak, A., Supported Transition Metal Phosphides: Activity Survey for HER, ORR, OER, and Corrosion Resistance in Acid and Alkaline Electrolytes. *ACS Catal.* **2019,** *9*, 11515-11529.

(10) Shi, Y.; Zhang, B., Recent Advances in Transition Metal Phosphide Nanomaterials: Synthesis and Applications in Hydrogen Evolution Reaction. *Chem. Soc. Rev.* **2016,** *45*, 1529-1541.

(11) Jiang, H.; He, Q.; Li, X.; Su, X.; Zhang, Y.; Chen, S.; Zhang, S.; Zhang, G.; Jiang, J.; Luo, Y., Tracking Structural Self-Reconstruction and Identifying True Active Sites toward Cobalt Oxychloride Precatalyst of Oxygen Evolution Reaction. *Adv. Mater.* **2019,** *31*, 1805127.

(12) Su, X.; Wang, Y.; Zhou, J.; Gu, S.; Li, J.; Zhang, S., Operando Spectroscopic Identification of Active Sites in NiFe Prussian Blue Analogues as Electrocatalysts: Activation of Oxygen Atoms for Oxygen Evolution Reaction. *J. Am. Chem. Soc.* **2018,** *140*, 11286-11292.

(13) Wygant, B. R.; Kawashima, K.; Mullins, C. B., Catalyst or Precatalyst? The Effect of Oxidation on Transition Metal Carbide, Pnictide, and Chalcogenide Oxygen Evolution Catalysts. *ACS Energy Lett.* **2018,** *3*, 2956-2966.

(14) An, L.; Feng, J.; Zhang, Y.; Wang, R.; Liu, H.; Wang, G. C.; Cheng, F.; Xi, P., Epitaxial Heterogeneous Interfaces on N-$NiMoO_4$/$NiS_2$ Nanowires/Nanosheets to Boost Hydrogen and Oxygen Production for Overall Water Splitting. *Adv. Funct. Mater.* **2019,** *29*, 1805298.

(15) Lin, J.; Wang, P.; Wang, H.; Li, C.; Si, X.; Qi, J.; Cao, J.; Zhong, Z.; Fei, W.; Feng, J., Defect-Rich Heterogeneous $MoS_2$/$NiS_2$ Nanosheets Electrocatalysts for Efficient Overall Water Splitting. *Adv. Sci.* **2019**, 1900246.

(16) Hu, C. Y.; Ma, Q. Y.; Hung, S. F.; Chen, Z. N.; Ou, D. H.; Ren, B.; Chen, H. M.; Fu, G.; Zheng, N. F., In Situ Electrochemical Production of Ultrathin Nickel Nanosheets for Hydrogen Evolution Electrocatalysis. *Chem* **2017,** *3*, 122-133.

(17) Ma, Q. Y.; Hu, C. Y.; Liu, K. L.; Hung, S. F.; Ou, D. H.; Chen, H. M.; Fu, G.; Zheng, N. F., Identifying the Electrocatalytic Sites of Nickel Disulfide in Alkaline Hydrogen Evolution Reaction. *Nano Energy* **2017,** *41*, 148-153.

(18) Zhang, Y.; Gao, L.; Hensen, E. J. M.; Hofmann, J. P., Evaluating the Stability of $Co_2P$ Electrocatalysts in the Hydrogen Evolution Reaction for Both Acidic and Alkaline Electrolytes. *ACS Energy Lett* **2018,** *3*, 1360-1365.

(19) Zhu, Y. P.; Chen, H. C.; Hsu, C. S.; Lin, T. S.; Chang, C. J.; Chang, S. C.; Tsai, L. D.; Chen, H. M., Operando Unraveling of the Structural and Chemical Stability of P-Substituted $CoSe_2$ Electrocatalysts toward Hydrogen and Oxygen Evolution Reactions in Alkaline Electrolyte. *ACS Energy Lett.* **2019,** *4*, 987-994.

(20) Zhai, L. L.; Mak, C. H.; Qian, J. S.; Lin, S. H.; Lau, S. P., Self-Reconstruction Mechanism in $NiSe_2$ Nanoparticles/Carbon Fiber Paper Bifunctional Electrocatalysts for Water Splitting. *Electrochim. Acta* **2019,** *305*, 37-46.

(21) Wang, F.; Li, Y.; Shifa, T. A.; Liu, K.; Wang, F.; Wang, Z.; Xu, P.; Wang, Q.; He, J., Selenium-Enriched Nickel Selenide Nanosheets as a Robust Electrocatalyst for Hydrogen Generation. *Angew. Chem. Int. Ed.* **2016,** *55*, 6919-6924.

(22) Kong, F. H.; Sun, L. P.; Huo, L. H.; Zhao, H., In-Situ Electrochemical Self-Tuning of Amorphous Nickel Molybdenum Phosphate to Crystal Ni-Rich Compound for Enhanced Overall Water Splitting. *J. Power Sources* **2019,** *430*, 218-227.

(23) Shang, X.; Dong, B.; Chai, Y. M.; Liu, C. G., In-Situ Electrochemical Activation Designed

Hybrid Electrocatalysts for Water Electrolysis. *Sci. Bull.* **2018,** *63*, 853-876.

(24) De las Heras, C.; Agulló-Rueda, F., Raman Spectroscopy of $NiSe_2$ and $NiS_{2-x}Se_x$ ($0< x< 2$) Thin Films. *J. Phys.: Condens. Matter* **2000,** *12*, 5317.

(25) Lin, J.; Wang, H.; Yan, Y.; Cao, J.; Qu, C.; Zheng, X.; Feng, J.; Qi, J., Sandwich-Like Structured $NiSe_2/Ni_2P$@ FeP Interface Nanosheets with Rich Defects for Efficient Electrocatalytic Water Splitting. *J. Power Sources* **2020,** *445*, 227294.

(26) Chang, A.; Zhang, C.; Yu, Y.; Yu, Y.; Zhang, B., Plasma-Assisted Synthesis of $NiSe_2$ Ultrathin Porous Nanosheets with Selenium Vacancies for Supercapacitor. *ACS Appl. Mater. Interfaces* **2018,** *10*, 41861-41865.

(27) Seh, Z. W.; Kibsgaard, J.; Dickens, C. F.; Chorkendorff, I.; Norskov, J. K.; Jaramillo, T. F., Combining Theory and Experiment in Electrocatalysis: Insights into Materials Design. *Science* **2017,** *355*, eaad4998.

(28) Qiu, B. C.; Wang, C.; Zhang, N.; Cai, L. J.; Xiong, Y. J.; Chai, Y., $CeO_2$-Induced Interfacial $Co^{2+}$ Octahedral Sites and Oxygen Vacancies for Water Oxidation. *ACS Catal.* **2019,** *9*, 6484-6290.

(29) Zhou, H. Q.; Wang, Y. M.; He, R.; Yu, F.; Sun, J. Y.; Wang, F.; Lan, Y. C.; Ren, Z. F.; Chen, S., One-Step Synthesis of Self-Supported Porous $NiSe_2$/Ni Hybrid Foam: An Efficient 3d Electrode for Hydrogen Evolution Reaction. *Nano Energy* **2016,** *20*, 29-36.

(30) Wang, P. Y.; Pu, Z. H.; Li, W. Q.; Zhu, J. W.; Zhang, C. T.; Zhao, Y. F.; Mu, S. C., Coupling $NiSe_2$-$Ni_2P$ Heterostructure Nanowrinkles for Highly Efficient Overall Water Splitting. *J. Catal.* **2019,** *377*, 600-608.

(31) Du, Y.; Cheng, G.; Luo, W., Colloidal Synthesis of Urchin-Like Fe Doped $NiSe_2$ for Efficient Oxygen Evolution. *Nanoscale* **2017,** *9*, 6821-6825.

(32) Mande, C.; Nigavekar, A., X-Ray Spectroscopic Study of Chemical Bonding in NiSe and

$NiSe_2$. *Proc. Indian Acad. Sci.*, Springer India, **1969**, 69, 316-323.

(33) Gu, C.; Hu, S.; Zheng, X.; Gao, M. R.; Zheng, Y. R.; Shi, L.; Gao, Q.; Zheng, X.; Chu, W.; Yao, H. B., Synthesis of Sub-2 nm Iron-Doped $NiSe_2$ Nanowires and Their Surface-Confined Oxidation for Oxygen Evolution Catalysis. *Angew. Chem. Int. Ed.* **2018,** *57*, 4020-4024.

(34) Dutta, S.; Indra, A.; Feng, Y.; Song, T.; Paik, U., Self-Supported Nickel Iron Layered Double Hydroxide-Nickel Selenide Electrocatalyst for Superior Water Splitting Activity. *ACS Appl. Mater. Interfaces* **2017,** *9*, 33766-33774.

(35) Folkerts, W.; Sawatzky, G. A.; Haas, C.; Degroot, R. A.; Hillebrecht, F. U., Electronic-Structure of Some 3d Transition-Metal Pyrites. *J. Phys. C.:Solid State* **1987,** *20*, 4135-4144.

(36) Moon, C.-Y.; Kang, H.; Jang, B. G.; Shim, J. H., Composition and Temperature Dependent Electronic Structures of $NiS_{2-x}Se_x$ Alloys: First-Principles Dynamical Mean-Field Theory Approach. *Phys. Rev. B* **2015,** *92*, 235130.

(37) Ataca, C.; Sahin, H.; Ciraci, S., Stable, Single-Layer $MX_2$ Transition-Metal Oxides and Dichalcogenides in a Honeycomb-Like Structure. *J. Phys. Chem. C.* **2012,** *116*, 8983-8999.

(38) Reyes-Retana, J. A.; Naumis, G. G.; Cervantes-Sodi, F., Centered Honeycomb $NiSe_2$ Nanoribbons: Structure and Electronic Properties. *J. Phys. Chem. C.* **2014,** *118*, 3295-3304.

(39) Yu, D.; Li, Z.; Zhao, G.; Zhang, H.; Aslan, H.; Li, J.; Sun, F.; Zhu, L.; Du, B.; Yang, B., Porous Ultrathin NiSe Nanosheet Networks on Nickel Foam for High-Performance Hybrid Supercapacitors. *ChemSusChem* **2020**, *13*, 260-266.

(40) Xu, B.; Chen, Z.; Yang, X.; Wang, X.; Huang, Y.; Li, C., Electronic Modulation of Carbon-Encapsulated NiSe Composites Via Fe Doping for Synergistic Oxygen Evolution. *Chem. Commun.* **2018**, *54*, 9075-9078.

(41) Nørskov, J. K.; Studt, F.; Abild-Pedersen, F.; Bligaard, T., The Electronic Factor in

Heterogeneous Catalysis. In *Fundamental Concepts in Heterogeneous Catalysis*, John Wiley & Sons, Inc: **2014**; pp 114-137.

(42) Wei, C.; Sun, Y.; Scherer, G. n. G.; Fisher, A. C.; Sherburne, M.; Ager, J. W.; Xu, Z. J., Surface Composition Dependent Ligand Effect in Tuning the Activity of Nickel–Copper Bimetallic Electrocatalysts toward Hydrogen Evolution in Alkaline. *J. Am. Chem. Soc.* **2020,** *142*, 7765-7775.

# Table of contents